remote sensing

MDPI

Technical Note

Underwater Temperature and Salinity Measurement by Rayleigh–Brillouin Spectroscopy Using Fizeau Interferometer and PMT Array

Yanpeng Zhao [1,2], Yuanqing Wang [3], Kun Liang [1,2,*], Yangrui Xu [1], Yuanxin Guo [1] and Kassim Makame [1]

[1] School of Electronic Information and Communications, Huazhong University of Science and Technology, Wuhan 430074, China; zhaoyanpeng@hust.edu.cn (Y.Z.); xuyangrui@hust.edu.cn (Y.X.); yux_g@hust.edu.cn (Y.G.); i202221044@hust.edu.cn (K.M.)
[2] National Key Laboratory of Multispectral Information Intelligent Processing Technology, Huazhong University of Science and Technology, Wuhan 430074, China
[3] School of Electrical and Information Engineering, Wuhan Institute of Technology, Wuhan 430205, China; 23121104@wit.edu.cn
* Correspondence: liangkun@hust.edu.cn

Abstract: This article presents a LiDAR system that utilizes a Fizeau interferometer and photomultiplier tube array to detect the water Rayleigh–Brillouin spectrum, utilized to obtain underwater temperature and salinity synchronizing measurements based on the Brillouin spectral linewidth and shift. Temperature and salinity measurements were conducted in the laboratory to verify the efficiency of the system. The results demonstrate that the LiDAR system can accurately obtain the Rayleigh–Brillouin spectral backscattering profiles of water. Following linear fitting and reconstruction, the retrieved temperature accuracy is ±0.13 °C and salinity accuracy is ±0.16‰. By effectively leveraging the multiparameter information contained in the Rayleigh–Brillouin spectrum, the system achieved precise temperature and salinity measurements. This study provides a reference for marine remote sensing applications

Keywords: underwater remote sensing; LiDAR; temperature; salinity; Rayleigh–Brillouin

Citation: Zhao, Y.; Wang, Y.; Liang, K.; Xu, Y.; Guo, Y.; Makame, K. Underwater Temperature and Salinity Measurement by Rayleigh–Brillouin Spectroscopy Using Fizeau Interferometer and PMT Array. *Remote Sens.* **2024**, *16*, 2214. https://doi.org/10.3390/rs16122214

Academic Editors: Cédric Jamet, Martin A. Montes, Junwu Tang and Peng Chen

Received: 7 May 2024
Revised: 14 June 2024
Accepted: 17 June 2024
Published: 19 June 2024

1. Introduction

The vertical distributions of marine temperature and salinity are crucial research subjects in the field of marine environmental science. These parameters play vital roles in analyzing ocean circulation patterns, understanding ocean currents, studying marine ecological composition, and investigating ecological changes [1–4]. Typically, temperature and salinity measurement methods can be divided into two categories: (1) direct measurement methods involving direct contact with the detection medium and (2) remote sensing detection methods, which involve the acquisition of information about an object or phenomenon without physical contact. Although direct detection methods have the advantages of high accuracy and rapid response [5–7], the requirement of in situ detection devices makes them unsuitable for continuous-range observations. Accordingly, remote sensing is becoming increasingly widespread in applications due to its wide detection range.

LiDAR, as a remote sensing technique, is being applied in marine remote sensing due to its strong adaptability to the environment and potential for spectral sensing. It has good penetrability and directivity for light emission in water [8–10]. The laser emitted by the LiDAR system undergoes scattering in water. The scattering spectrum comprises an elastic component, called Rayleigh scattering, and fluctuations in the water density cause nonelastic scattering of the laser. This results in a frequency shift compared with the laser source frequency, which produces a Stokes peak and an anti-Stokes peak, known as the Brillouin scattering spectrum [11]. When the temperature and salinity change, the Rayleigh–Brillouin scattering spectrum exhibits a different curve. Temperature and salinity

information can be extracted by analyzing the distinct peaks in the Rayleigh–Brillouin scattering spectrum of water [12,13]. Because the linewidths of both the Brillouin and Rayleigh peaks are narrow, sampling and analyzing the spectrum is difficult [14]. Moreover, owing to the strong attenuation in water, the signal-to-noise ratio (SNR) of the received signal is very low, which makes it difficult to detect narrow linewidths of the Brillouin scattering spectrum. To overcome these challenges, several studies have been conducted on water-scattering detection systems.

To obtain the Rayleigh–Brillouin scattering spectrum of water, Emery et al. used a scanning Fabry–Perot (FP) interferometer to obtain a complete scattering spectrum. However, this time-consuming scanning process is difficult to use in practical applications [15]. To obtain the real-time spectral information, Popeescu et al. determined the positions of the Brillouin double peaks in the backscattering spectrum by measuring the absorption peaks of the molecular absorption pool [16]. This detection method sacrifices the acquisition of other spectral information to obtain real-time, specific Rayleigh–Brillouin spectral features. However, the detection and inversion accuracies are significantly reduced when the SNR is lowered, due to various uncertainty factors in the water. Shi et al. used the FP standard to change the cavity length dynamically and display different frequency–domain points on the image plane of an intensified charge-coupled device. This method can achieve a high temporal resolution; however, it is not easy to denoise and extract spectral information from the holographic ring [17]. Wang et al. proposed a method to detect the underwater Brillouin frequency shift and inversion of temperature and salinity using a dual-step FP [18]. In this method, a Brillouin frequency shift of less than 4.3 MHz and Brillouin linewidth of 3.2 MHz yielded an inversion accuracy of 0.1 °C temperature and 0.5‰ salinity. However, because the dual-step FP is used as an optical frequency discriminator, a small disturbance, such as a laser frequency or external ambient temperature change, may cause a low SNR or incorrect result. Therefore, it is necessary to calibrate the laser wavelength before system data acquisition to achieve a high data acquisition accuracy for each measurement.

Considering the disadvantages of the dual-step FP method, a method combining a Fizeau interferometer with a photomultiplier tube (PMT) array was previously proposed [19]. In this method, the problem of absolute frequency instability can be overcome, because it can accurately determine the relative frequency. In this manner, a modelling temperature and salinity accuracy of 0.5 K and 1‰ within an underwater detection distance of 40.51 m can be achieved. This detection method has already been used in real applications for atmospheric environmental parameter detection by Xu et al. in 2021. A temperature inversion of 2 K was obtained, which demonstrates that this detection method can effectively avoid the above-mentioned problems in using dual-step PMT array detection [20]. Although the attenuation of light in water is significantly stronger than that in the atmosphere and there are more uncertain environmental noise interferences, Xu's study provides new insights into underwater Rayleigh–Brillouin spectrum detection.

In 2021, Xu analyzed the influence of temperature, salinity, and depth of the upper ocean on the frequency shift of the Brillouin LiDAR. Their experimental results showed that the Brillouin frequency shift varied from 7.483 to 7.812 GHz in a pressure range of 0–2 MPa [21]. According to Xu, the selection of a Fizeau interferometer with an appropriate spectral range enables comprehensive acquisition of the Brillouin scattering spectrum, thereby facilitating the detection of ocean temperature and salinity. In contrast to the atmosphere, the Brillouin scattering peaks in water are independent, which makes this technology more promising for potential applications. Based on previous simulation research, a remote-sensing LiDAR system for measuring the Rayleigh–Brillouin scattering spectrum of water was constructed in this study. The crucial parts of the system are the Fizeau interferometer and PMT array. A Fizeau interferometer was used as the high-precision optical frequency discriminator to obtain the complete Rayleigh and Brillouin scattering spectra of water. A PMT array was used to convert and acquire the spectral and sample signals. Using this system, the discrete Rayleigh–Brillouin spectrum of water was

measured. After the spectrum was reconstructed by curve fitting, the temperature and salinity information of the water were retrieved.

2. Method and Experiment

2.1. Water Temperature and Salinity

When a laser beam enters water, it interacts with water molecules, resulting in scattering signals. In general, the scattering profile reflects the motion of molecules, which is closely related to the molecular environment, as shown in Figure 1. Rayleigh–Brillouin scattering (RBS) manifests as two features: a Doppler-broadened central Rayleigh peak and two Stokes- and anti-Stokes-shifted Brillouin peaks. The RBS line shape can be interpreted as a linear combination of the Rayleigh peak and Brillouin doublet [22]. In the case of water, scattering predominantly occurred in the hydrodynamic region, where the Rayleigh peak was completely separated from the Brillouin peaks. These peaks can be described mathematically using three Lorentzian functions [23–25].

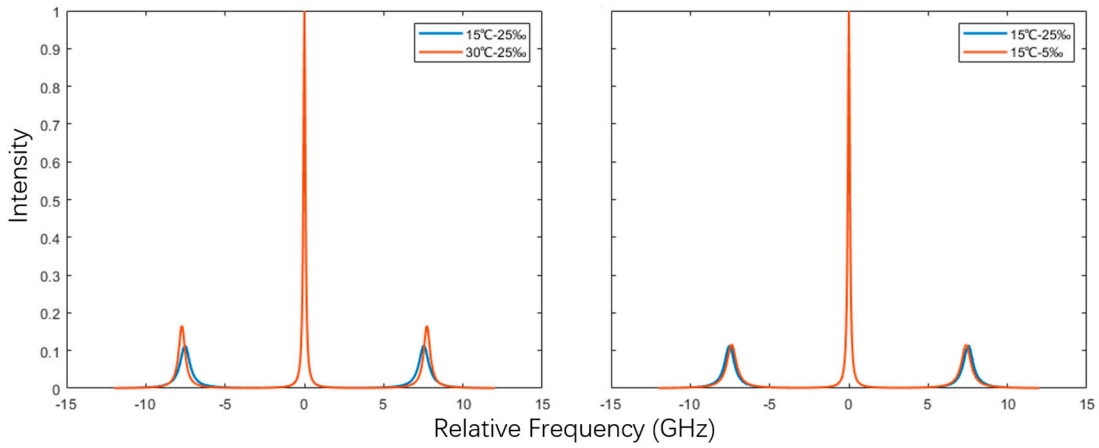

Figure 1. Typical Brillouin scattering spectrum changes with different temperatures (**left**) and salinity (**right**).

According to Yu, the temperature and salinity of water can be obtained by analyzing the Brillouin linewidth and frequency shift [26]. Therefore, spectral acquisition should be completed first for environmental parameter detection. In this study, a Fizeau interferometer in conjunction with a PMT array was employed to capture the scattered echo spectrum; the acquisition process is illustrated in Figure 2.

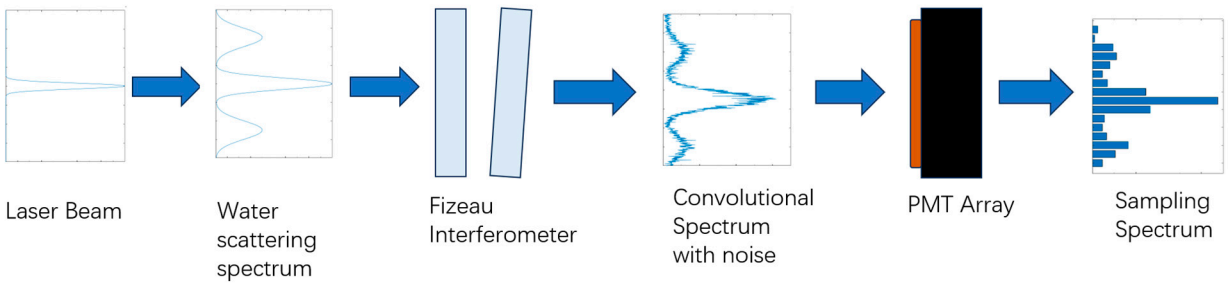

Figure 2. Method of spectrum sampling.

As shown in Figure 2, the laser beam penetrates water and generates backward Rayleigh–Brillouin scattering light. The backscattered signal then passes through a Fizeau interferometer, which serves as a frequency discriminator and generates a frequency-domain spectral signal. The spectrum exhibits a continuous distribution with the Rayleigh signal positioned at the center and two symmetrical Brillouin peaks located on either side of the central peak. Subsequently, a continuous spectral signal was captured by a 16-channel

PMT array that was evenly distributed among the sampled channels. Furthermore, the original backscattered signal spectrum can be reconstructed by performing linear fitting with the sampled Rayleigh–Brillouin scattering photons.

2.2. Experimental Apparatus

To obtain high-precision water temperature and salinity information, a LiDAR system was constructed to detect the Brillouin linewidth and Brillouin frequency shift, as shown in Figure 3.

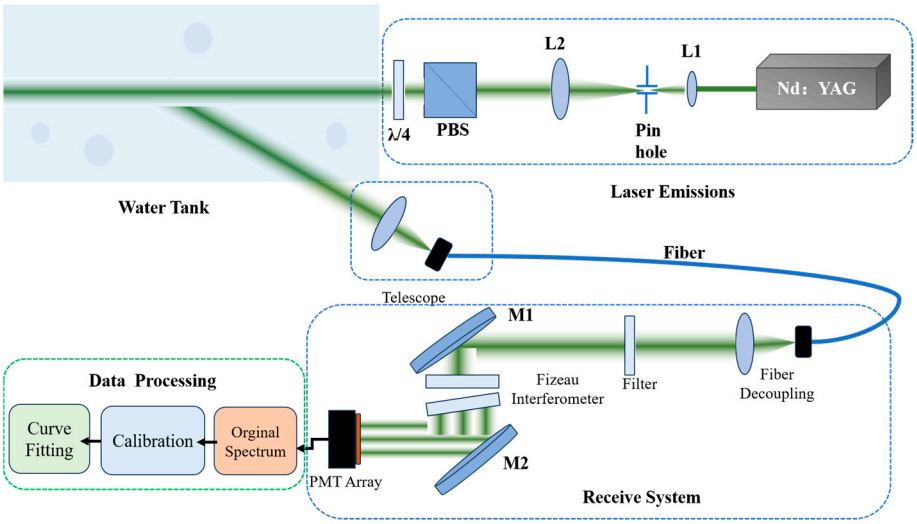

Figure 3. LiDAR system for underwater temperature and salinity measurement. Nd:YAG is a pulsed laser source; L1 and L2 are lens with focal lengths of 25.4 mm and 50.8 mm, respectively; PBS is a polar beam splitter cube; λ/4 is a quarter-wave plate; and M1 and M2 are reflectors.

In Figure 3, the laser source produces a narrowed single-frequency light. The light was then passed through a beam expander with a pinhole that provides 2× magnification and then directly placed into a sealed stationary water tank after applying an optical isolator (comprising a PBS and quarter-wave plate). The echo scattering light was captured by the receiving telescope with aperture diameter φ_1 = 25.4 mm and focal length F_1 = 75 mm. The photographs received by the telescope were transmitted by an optical fiber with a numerical aperture NA_F = 0.22. The photons were then collimated by a fiber decoupler with aperture diameter φ_2 = 50.8 mm and focal length F_2 = 100 mm. After collimation, beam expansion, and filtering, the backscattered light spectrum was transmitted to the Fizeau interferometer for frequency selection and then sampled by a PMT array. The obtained photocurrent signal was subjected to channel differential correction and removal of random noise and dark noise, followed by determination of the pixel resolution. Finally, curve fitting was performed to extract the desired Brillouin frequency shifts and linewidths. For the detailed system parameters, refer to Table 1.

Table 1. System parameters of the LiDAR.

Parameter Name	Value
PRF (Hz)	100
Pulse time (ns)	7.5
Wavelength (nm)	532
Laser power@532 nm (mJ)	20 ± 1
System efficiency (%)	80
Telescope focus (mm)	100
Quantum efficiency (%)	17.6
PMT array	SPCM-02-L16-110

The laser was directed into a closed water tank with a size of 1.8 × 0.65 × 0.4 m (length × width × height). To minimize the influence of reflection from the water tank surface, the laser was directed towards the closed water at 165.8°. To ensure clear and representative Brillouin signals, the electrical conductivity of the water used in the tank was 1.56 at (25 °C ± 1 °C)/(μS/cm). Additionally, a temperature controller was used to control the temperature of the water in the tank, maintaining it within a change range of no more than ±0.3 °C.

2.2.1. Light Source

In previous studies, it was found that the salinity error induces a Brillouin frequency shift in water within the range of ±1 MHz was 0.84‰, while the water temperature affects the Brillouin linewidth within a range of ±1 MHz, with a dependency of 0.06 K [27]. To achieve high accuracy in temperature and salinity inversion, the system utilizes a seed-injected, high-stability-frequency pulsed laser. Considering that water has a high attenuation of ultraviolet frequencies [19,28], the center frequency of the light source used in this study was 532 nm. The frequency drift of the laser under short-term operating conditions was less than 7 MHz, whereas that under long-term operating conditions was less than 10 MHz, which meets the requirements for detection accuracy.

2.2.2. Telescope and Optical Path

A lens with a diameter of 25.4 mm and focal length of 75 mm was used in this setup as the receiving telescope. To minimize signal attenuation in the laboratory setting, a multimode optical fiber with a numerical aperture of 0.22 NA and diameter of 200 μm was used to couple and transmit the received echo signals from the telescope. Additionally, another lens with 50.8 mm diameter and a focal length of 100 mm helped achieve a suitable spot size and compressed the outgoing divergence angle, ensuring that the incident rays were collimated and diverged within an appropriate range before entering the interferometer.

2.2.3. Spectrum Acquisition Module

A Fizeau interferometer was used in the LiDAR system to obtain comprehensive and precise scattering echo spectrum information across a wide frequency range. This interferometer comprised two wedge-shaped optical plates with an air medium in between, allowing the generation of uniform interference fringes based on the principle of equal-thickness interference. The free spectral range and full width at half maximum (FWHM) of the interferometer were 25 GHz and 1.45 GHz, respectively, which can fully represent the range of the Rayleigh–Brillouin scattering spectrum of water and accurately represent the Brillouin frequency shift and line width.

Scattered light can only be received and processed after conversion using a photoelectric converter. As the CCD is limited by a long exposure time, the PMT can compensate for the shortcomings of the CCD in terms of time resolution, owing to its higher response speed. According to Wang's research, when the number of PMT sampling points reaches 12 or more, a Brillouin linewidth and Brillouin frequency shift accuracy of 2 MHz and temperature and salinity inversion accuracy of 0.5 K and 1‰, respectively, can be obtained [19]. Therefore, a 16-channel PMT array (SPCM-02-L16, HOLITA) with 6.5 × 10^4 A/W was selected for the sample spectrum. Moreover, an acquisition system with a sampling rate of 5000 MHz was used for optoelectronic signal conversion.

2.2.4. Data Calibration

In the presence of water attenuation and various noise components [29], the SNR of a single sampling signal is low, making it difficult to clearly distinguish the Brillouin spectrum distribution in water. Among them, the noise caused by the nonuniformity of the PMT is an important factor affecting the spectral accuracy. Because of the specificity of the cathode material of the PMT array, the photo sensitivities of different channels are not at exactly the same level [30,31].

As the diffuse reflection signal from a filament lamp can be considered as a uniform light signal, to perform the non-uniform correction, a tungsten filament lamp operated at 2856 K was employed to compensate for the differences in response coefficients among the PMT channels.

The maximum value of each channel and its ratio to the maximum value of the 16th channel, as shown in Figure 4, were used as the special correction coefficient, c_i. The original data for each channel, x_i, were then divided by the correction coefficient to obtain signal x_{ic} after correction, as follows:

$$x_{ic} = x_i \div c_i. \tag{1}$$

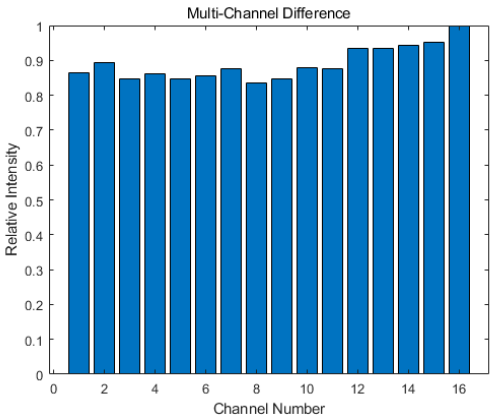

Figure 4. PMT channel photosensitivity differential coefficient.

An approach was implemented in this study to mitigate the influence of dark noise on the signals. During the initial phase of the signal acquisition, the clock of the data acquisition system was deliberately set to lead the laser pulse, resulting in the collection of a dark-noise floor signal. This dark-noise floor signal served as a reference for correcting the dark noise.

For each of the 16 channels, a section of the reference dark-noise signal was extracted from the beginning of the signal. The average value of the reference dark noise was then calculated. To remove the dark noise from the overall signal of each channel, the calculated reference dark noise value was subtracted from the corresponding channel signal.

After obtaining the smoothed average signal, the pixel resolution for each channel was determined. This was achieved by illuminating the PMT cathode with an attenuated reference laser signal, which allowed the acquisition of the 16-channel distribution of the interferometer instrument function. By altering the laser frequency, the positions of the interference fringes on the PMT channel exhibited a linear variation. Figure 5 shows that typical interference fringes move when the laser frequency changes.

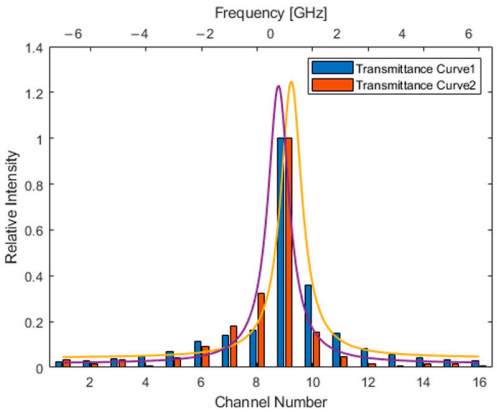

Figure 5. Fizeau transmittance curve with a laser frequency change of 0.7 GHz.

To determine the pixel resolution of the LiDAR system, we changed the laser frequency ten times and recorded the center of the transmittance curve. The results are shown in Figure 6.

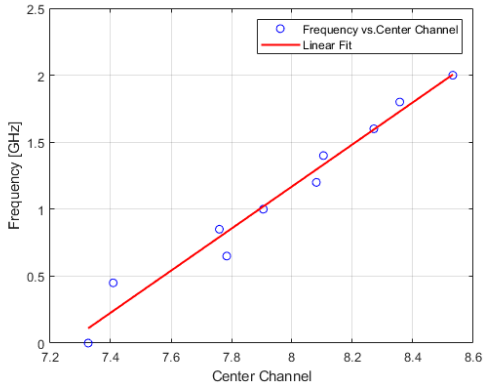

Figure 6. Transmittance curve center channel with different laser frequencies.

In Figure 6, the y-axis represents the deviation of the laser center frequency from the standard value, and the x-axis represents the change in the position of the fringe center. By performing a linear fit on the obtained results, a linear relationship between the center channel and laser center frequency variation can be obtained. The slope of the fitted curve represents the pixel resolution. From the graph, the system's pixel resolution was estimated as 1.571 ± 0.082 GHz, allowing for a frequency domain range of 25.136 GHz for the 16 channels. Utilizing the frequency-position relationship of each channel, the entire linear model was fitted using the three Lorentz linear models. The center and FWHM of the Lorentz lines on both sides of the center represent the frequency shift and linewidth of the Brillouin scattering spectrum, respectively.

3. Results

To achieve accurate measurements of water temperature and salinity in the laboratory environment, a temperature control system was employed to monitor and modify the temperature of the laboratory water.

Following the acquisition of the experimental water data by the system, the temperature of the water was measured using a direct-contact thermometer with an accuracy of ±0.1 °C and used as the reference water temperature in the laboratory environment. Any changes in the experimental water temperature during the observation period were disregarded or considered negligible.

3.1. Original Data from the LiDAR System

The original data acquired by the LiDAR system are shown in Figure 7. The 16 channels in the image represent the complete water-scattering spectrum. However, the Brillouin peaks were opaque, baseline noise levels were inconsistent, and there was considerable noise.

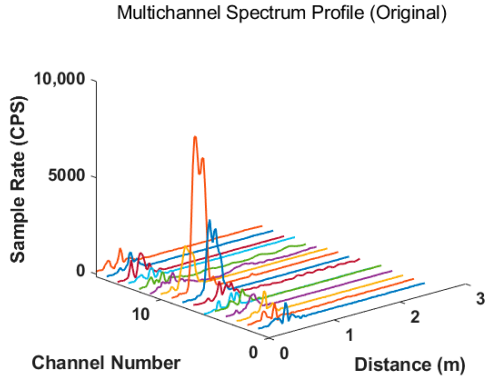

Figure 7. Original data at a temperature of 25.1 °C and salinity of 0.1‰.

3.2. Channel Geometric Difference Correction

To address channel geometric differences, a correction method based on the c_i values described in Section 2.2.4 was employed in this study. Figure 8 shows the results of the channel difference correction. By applying channel-specific signal correction to Equation (1), the errors caused by uneven channel response could be effectively reduced.

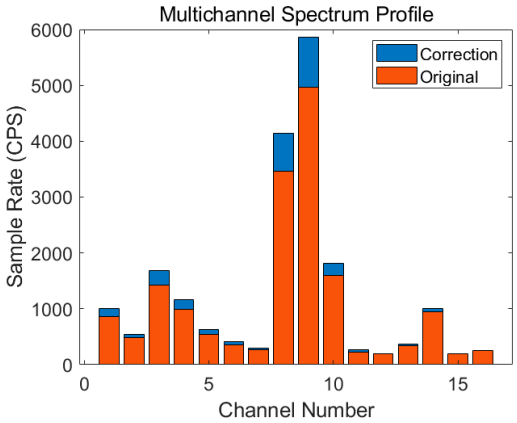

Figure 8. Channel difference correction result.

3.3. Dark Current Correction Result

The uneven distribution of the baseline noise levels in each channel can be attributed to several factors. First, the PMT operates at high voltages and the stability of the PMT's first dynode is affected by the power supply ripple, leading to fluctuations in the magnitude of the photocurrent.

Additionally, the PMT signals were not directly output to the acquisition equipment but passed through a transimpedance amplifier, which introduces its own output noise. This noise varies with changes in the input signal. Moreover, the bias current of the transimpedance amplifier is combined with the anode dark current generated by the spontaneous transition of the photocathode electrons, resulting in the coupling of the system dark noise to the signal in the form of a DC component.

To correct for dark noise, a reference section of dark noise was captured at the beginning of each of the 16 channels where no laser signal was present. The elimination of dark noise from the overall signal of each channel results in a signal without dark noise. The results obtained after removing baseline noise from the two channels are shown in Figure 9.

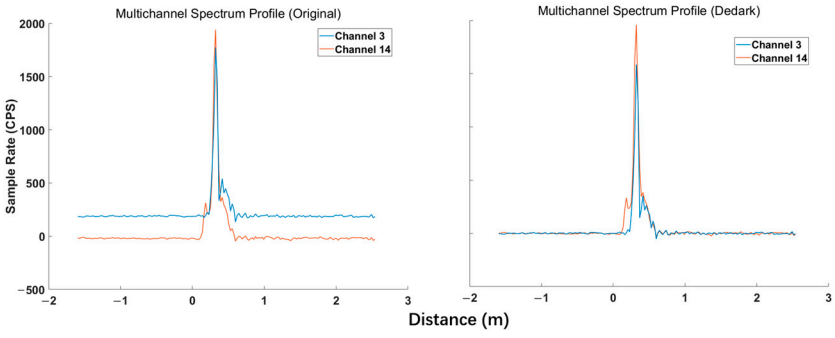

Figure 9. Signal dark current removed before (**left**) and after (**right**).

As shown in Figure 9, after the removal of dark current noise, the DC component of the two-channel signal was adjusted to zero. However, the fluctuations in the signal remained significant.

3.4. Spectrum Signal Integration Result

The result after cumulative averaging of random noise removal is shown in Figure 10.

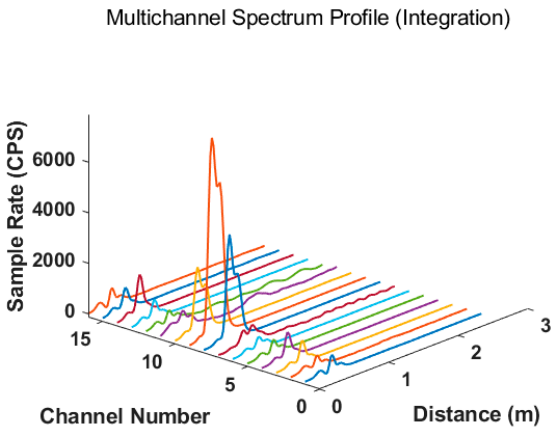

Figure 10. Spectrum with 1000 times integration vs. distance from excitation source.

From Figure 10, it can be observed that, compared to the raw signal in Figure 7, the signal curve of each channel becomes smooth and the spectrum distribution becomes clearer after cumulative averaging. Slicing Figure 10 at x = 0.36 m and normalizing the area yields a distinct Rayleigh signal, and symmetric Brillouin peaks on both sides and half of the Brillouin peaks on both sides can be presented on the 16 channels. The central Rayleigh signal was located on the ninth channel of the PMT array. It is evident that the processed signal can clearly identify the central Rayleigh signal and symmetric Brillouin signal on both sides, as shown in Figure 11.

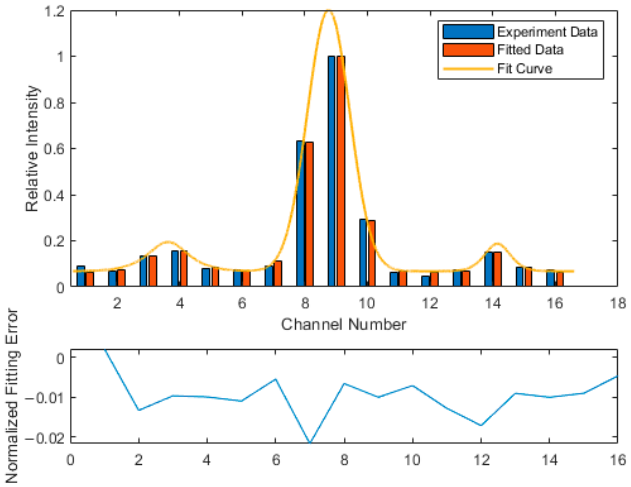

Figure 11. Three Lorentzian fitting result for PMT-acquired signals.

Moreover, to obtain the complete Rayleigh–Brillouin spectrum, three Lorentzian models were used to fit the central free-spectrum range. It can be seen that after certain calibration, good fitting results can be achieved with the three Lorentzian linear models. The Brillouin frequency shift was obtained by extracting the center positions of the Lorentzian linear models obtained from fitting on both sides and taking the arithmetic average. The Brillouin linewidth can be obtained by extracting the FWHM of the Lorentzian linear models, as shown in Figure 12.

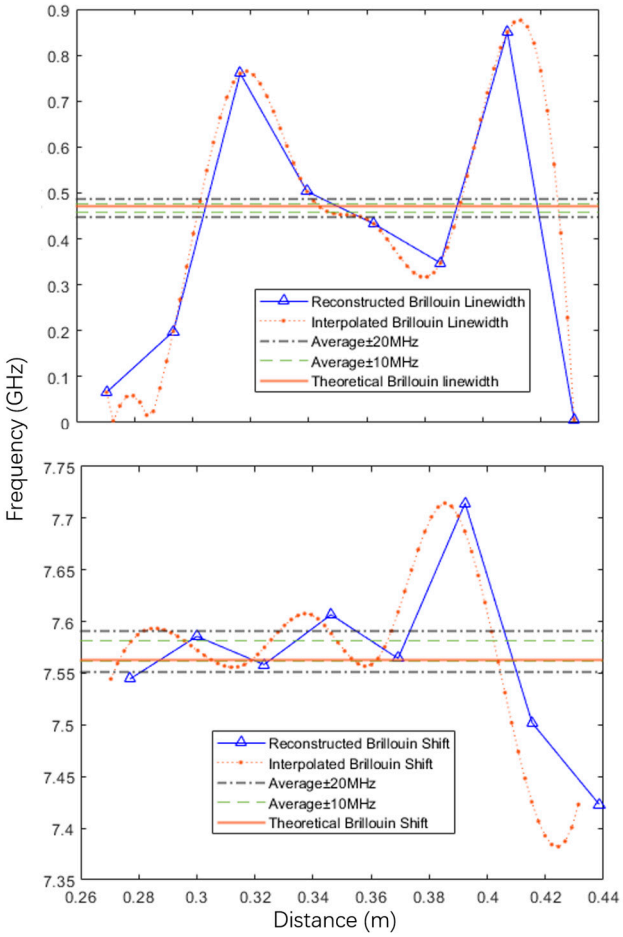

Figure 12. Brillouin linewidth (**top**) and Brillouin shift (**bottom**) vs. integrated groups.

3.5. Temperature and Salinity Inversion Result

Figure 12 shows the fitted results of the Brillouin linewidth (top) and Brillouin shift (bottom) obtained from Lorentzian linear fitting at a temperature of 25.1 °C and salinity of 0.1‰. It should be noted that, because of the inability to achieve strictly normal incidence, we could only ensure that the incident light was within an incidence angle of less than 0.5° to reduce the asymmetric impact caused by multilevel interference. Therefore, the Brillouin frequency shift and linewidth shown in Figure 12 are the average values of the fitting results for both sides. As shown in Figure 12, the fitted Brillouin linewidth of the Brillouin peaks on both sides of the central Rayleigh peak yielded a value of 0.481 GHz. The analysis of the Brillouin shift is shown in Figure 12, where the result of 1000 integrations is relatively stable and the average Brillouin shift is 7.56 GHz. By performing an arithmetic mean analysis on the fitting results of the peak region of the echo signal, it was observed that the error between the fitted results and standard reference value was within 10 MHz.

The temperature and pressure results were obtained by substituting the fitted values of the Brillouin shift and linewidth into the temperature and salinity inversion model [26], as shown in Figures 13 and 14.

To validate the accuracy and stability of the system for temperature measurements, we utilized a temperature control device to increase the water temperature and maintain its stability. We collected a total of five echo signals at temperatures of 19.1 °C, 20.8 °C, 24.5 °C, 25.1 °C, and 29.8 °C and a salinity concentration of 0.1‰. In Figure 13, M represents the integral number. These signals were subjected to signal processing and inversion, resulting in the performance of the system at different temperatures, as shown in Figure 13. Individual echo signals exhibited higher inversion errors because of their lower signal-to-

noise ratios. However, as the number of integrations gradually increased, the temperature inversion errors began to converge.

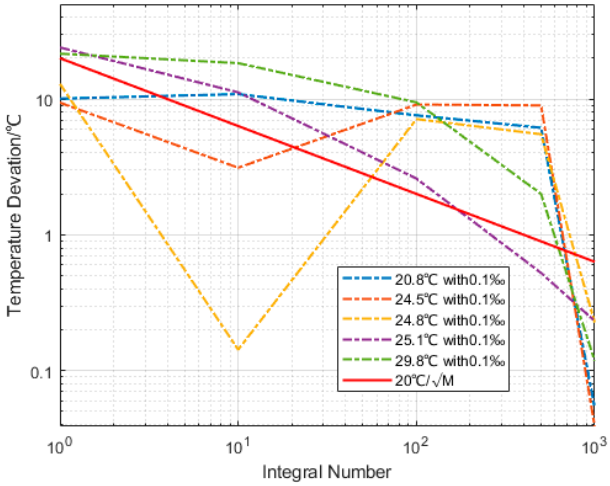

Figure 13. Absolute deviation in temperature between retrieved values and real values at different average values for water temperature and salinity in five groups of experiments.

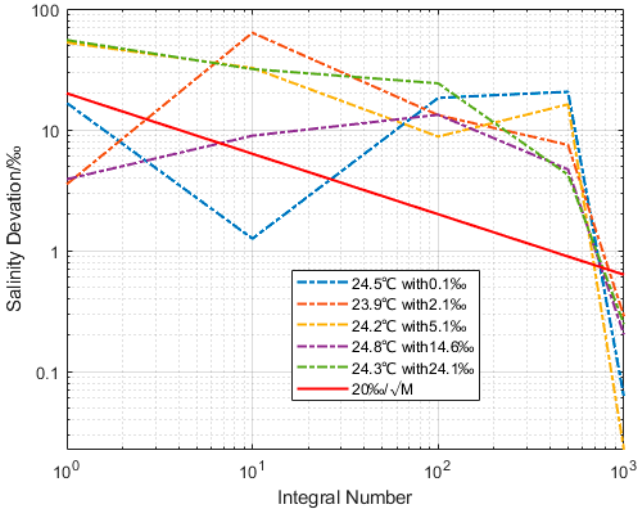

Figure 14. Absolute deviation in salinity between retrieved values and real values at different average numbers for the water in five groups of experiments.

Figure 13 shows that when the number of integrations reaches 1000, the inversion results for the five reference temperatures can achieve an accuracy of ±0.13 °C, with a maximum error of ±0.23 °C and a minimum error of ±0.04 °C.

To validate the accuracy and stability of the system for salinity measurements, salt was added to the water in batches to ensure thorough mixing and sufficient dissolution. We collected a total of five echo signals at salinity levels of 0.1‰, 2.1‰, 6.2‰, 5.1‰, and 24.1‰. These signals were subjected to signal processing and inversion, yielding the performance of the system at different salinity levels, as shown in Figure 14. Individual echo signals exhibited higher inversion errors because of their lower SNRs. Similarly, as the number of integrations gradually increases, the salinity inversion errors begin to converge.

From Figure 14, it appears that when the number of integrations reaches 1000, the inversion results for the five reference salinity levels can achieve an accuracy of ±0.16‰, with a maximum error of ±0.29‰ and a minimum error of ±0.02‰.

4. Conclusions

To measure the underwater temperature and salinity, a LiDAR that can resolve the Rayleigh–Brillouin spectrum of scattered light was constructed in this study. In this system, a Fizeau interferometer serves as an optical frequency discriminator, combined with a PMT array for optoelectronic signal conversion. This system can measure the full Rayleigh–Brillouin spectrum with a frequency resolution of 0.7854 GHz. To test the performance of the LiDAR system, experiments were conducted in a laboratory environment under different conditions. By denoising and curve fitting, the system could detect a relatively comprehensive Rayleigh–Brillouin scattering spectrum and achieve a temperature accuracy of ±0.13 °C and salinity accuracy of ±0.16‰ through nonlinear fitting of the spectrum using three Lorentz models.

The experiment further verified the strong dependence of the Brillouin frequency shift and linewidth on the temperature and salinity of water and demonstrated the reliability of using a Fizeau interferometer combined with a PMT array for the acquisition and analysis of Rayleigh–Brillouin scattering signals in water. In this system, the PMT can only work in a normally open state, and the echo signal at a single moment is easily contaminated by noise as well as at other times. In addition, to achieve continuous and stable results, it is necessary to operate the interferometer in a suitable environment, which requires stable external piezoelectric control and an appropriate temperature. During the research process, it is common to encounter situations in which the data inversion results are not ideal, due to the instability of the interferometer. In the future, the Fizeau interferometer will be modified to use a power supply with a smaller ripple and will also adopt an efficient temperature control system. A gate signal can be added to improve the SNR. Moreover, a PMT with dynamic gain is considered to realize large dynamic range detection. Additionally, more stable interferometer piezoelectric control solutions and temperature control systems should be adopted to achieve stable long-term observations. In future practical applications, we will consider referring to the single-photon design idea to conduct marine field exploration [32,33]. This achieves the purpose of large-dynamic-range observations.

Author Contributions: Conceptualization: K.L. and Y.W.; methodology: Y.Z.; software: Y.X.; validation: Y.Z., Y.X. and K.M.; formal analysis: K.M.; investigation: Y.G.; resources: K.L.; data curation: K.M.; writing—original draft preparation: Y.Z.; writing—review and editing: Y.W.; visualization: Y.Z.; supervision: K.L.; project administration: K.L.; funding acquisition: K.L. All authors have read and agreed to the published version of the manuscript.

Funding: This research was funded by the pre-research Project on Civil Aerospace Technologies (D040107).

Data Availability Statement: Data available on request due to restrictions.

Conflicts of Interest: The authors declare no conflicts of interest.

References

1. Kumar, A.; Wang, H.; Xue, Y. How much of monthly subsurface temperature variability in the equatorial Pacific can be recovered by the specification of sea surface temperatures? *J. Clim.* **2014**, *27*, 1559–1577. [CrossRef]
2. Kordas, R.L.; Harley, C.D.; O'Connor, M.I. Community ecology in a warming world: The influence of temperature on interspecific interactions in marine systems. *J. Exp. Mar. Biol. Ecol.* **2011**, *400*, 218–226. [CrossRef]
3. Dahlhoff, E.P. Biochemical indicators of stress and metabolism: Applications for marine ecological studies. *Annu. Rev. Physiol.* **2004**, *66*, 183–207. [CrossRef]
4. Röthig, T.; Trevathan-Tackett, S.M.; Voolstra, C.R. Human-induced salinity changes impact marine organisms and ecosystems. *Glob. Chang. Biol.* **2023**, *29*, 4731–4749. [CrossRef]
5. Huang, X.; Pascal, R.W.; Chamberlain, K. A miniature, high precision conductivity and temperature sensor system for ocean monitoring. *Sens. J.* **2011**, *11*, 3246–3252. [CrossRef]
6. Zhao, Y.; Wu, Q.L.; Zhang, Y.N. Simultaneous measurement of salinity, temperature and pressure in seawater using optical fiber SPR sensor. *Measurement* **2019**, *148*, 106792. [CrossRef]

7. Amiri, I.S.; Paul, B.K.; Ahmed, K. Tri-core photonic crystal fiber based refractive index dual sensor for salinity and temperature detection. *Microw. Opt. Technol. Lett.* **2019**, *61*, 847–852. [CrossRef]
8. Yueh, S.H.; Chaubell, J. Sea surface salinity and wind retrieval using combined passive and active L-band microwave observations. *Geosci. Remote Sens.* **2012**, *50*, 1022–1032. [CrossRef]
9. Liu, Q.; Liu, D.; Zhu, X. Optimum wavelength of spaceborne oceanic lidar in penetration depth. *J. Quant. Spectrosc. Radiat. Transf.* **2020**, *256*, 107310. [CrossRef]
10. Chen, S.; Xue, C.; Zhang, T. Analysis of the optimal wavelength for oceanographic lidar at the global scale based on the inherent optical properties of water. *Remote Sens.* **2019**, *11*, 2705. [CrossRef]
11. Lavrentieva, N.N. Semiempiric approach for line broadening and shifting calculation. In Proceedings of the 14th Symposium on High-Resolution Molecular Spectroscopy, Krasnoyarsk, Russia, 6–11 July 2003; Volume 5311, pp. 208–218.
12. Fry, E.S.; Emery, Y.; Quan, X. Accuracy limitations on Brillouin lidar measurements of temperature and sound speed in the ocean. *Appl. Opt.* **1997**, *36*, 6887–6894. [CrossRef]
13. Parker, T.R.; Farhadiroushan, M.; Handerek, V.A. A fully distributed simultaneous strain and temperature sensor using spontaneous Brillouin backscatter. *IEEE Photonics Technol. Lett.* **1997**, *9*, 979–981. [CrossRef]
14. Pan, X.; Shneider, M.N.; Miles, R.B. Coherent Rayleigh-Brillouin scattering in molecular gases. *Phys. Rev. A* **2004**, *69*, 2–5. [CrossRef]
15. Emery, Y.; Fry, E.S. Laboratory development of a LIDAR for measurement of sound velocity in the ocean using Brillouin scattering. *Ocean. Opt. XIII. Int. Soc. Opt. Photonics* **1997**, *2963*, 210–215.
16. Popescu, A.; Walther, T. On an ESFADOF edge-filter for a range resolved Brillouin-lidar: The high vapor density and high pump intensity regime. *Appl. Phys.* **2010**, *98*, 667–675. [CrossRef]
17. Shi, J.; Ouyang, M.; Gong, W. A Brillouin lidar system using F–P etalon and ICCD for remote sensing of the ocean. *Appl. Phys. B* **2008**, *90*, 569–571. [CrossRef]
18. Wang, Y.; Zhang, J.; Zheng, Y. Brillouin scattering spectral for liquid detection and applications in oceanography. *Opto-Electron. Adv.* **2023**, *220016*, 7–8.
19. Wang, Y.; Xu, Y.; Chen, P.; Liang, K. Remote Sensing of Seawater Temperature and Salinity Profiles by the Brillouin Lidar Based on a Fizeau Interferometer and Multichannel Photomultiplier Tube. *Sensors* **2022**, *23*, 446. [CrossRef]
20. Xu, J.; Witschas, B.; Kabelka, P.G.; Liang, K. High-spectral-resolution lidar for measuring tropospheric temperature profiles by means of Rayleigh–Brillouin scattering. *Opt. Lett.* **2021**, *46*, 3320–3323. [CrossRef]
21. Ning, X.; Liu, Z.; Zhang, X. Influence of temperature-salinity-depth structure of the up-per-ocean on the frequency shift of Brillouin LiDAR. *Opt. Express* **2021**, *29*, 36442–36452.
22. Yong, M.; Hao, L.; Gu, Z. Analysis of Rayleigh-Brillouin spectral profiles and Brillouin shifts in nitrogen gas and air. *Opt. Express* **2014**, *22*, 2092–2104.
23. Young, A.T. Rayleigh scattering. *Appl. Opt.* **1981**, *20*, 533–535. [CrossRef]
24. Young, A.T.; Kattawar, G.W. Rayleigh-scattering line profiles. *Appl. Opt.* **1983**, *22*, 3668–3670. [CrossRef]
25. Liang, K.; Ma, Y.; Huang, J. precise measurement of Brillouin scattering spectral in the ocean using F–P etalon and ICCD. *Appl. Phys. B* **2011**, *105*, 421–425. [CrossRef]
26. Yu, Y.; Ma, Y.; Li, H. Simulation on simultaneously obtaining ocean temperature and salinity using dual-wavelength Brillouin Lidar. *Laser Phys. Lett.* **2014**, *11*, 6–7. [CrossRef]
27. Duntley, S.Q. Light in the sea. *J. Opt. Soc. Am.* **1963**, *53*, 214–233. [CrossRef]
28. Sullivan, S.A. Experimental study of the absorption in distilled water, artificial sea water, and heavy water in the visible region of the spectral. *J. Opt. Soc. Am.* **1963**, *53*, 962–968. [CrossRef]
29. Ma, Y.; Fan, F.; Liang, K. An analytical model for Rayleigh–Brillouin scattering spectra in gases. *J. Opt.* **2012**, *14*, 095703. [CrossRef]
30. Neves, F.; Chepel, V.; Akimov, D.Y. Calibration of photomultiplier arrays. *Astropart. Phys.* **2010**, *33*, 13–18. [CrossRef]
31. Kalousis, L.N.; De André, J.P.A.M.; Baussan, E. A fast numerical method for photomultiplier tube calibration. *J. Instrum.* **2020**, *15*, P03023. [CrossRef]
32. Shangguan, M.; Yang, Z.; Lin, Z. Full-day profiling of a beam attenuation coefficient using a single-photon underwater lidar with a large dynamic measurement range. *Opt. Lett.* **2010**, *49*, 626–629. [CrossRef]
33. Shangguan, M.; Yang, Z.; Lin, Z. Compact long-range single-photon underwater lidar with high spatial-temporal resolution. *IEEE Geosci. Remote Sens. Lett.* **2023**, *20*, 1501905. [CrossRef]